minerals

MDPI

Article

Path-Dependent Diagenesis and Facies-Controlled Reservoir Quality in Lower Cretaceous Fan-Delta Sandstones, North Yellow Sea Basin: A Model for Superimposed Rift Basins

Xiaoqiang Yuan [1,2], Jinping Liu [1,2,*], Gaiyun Wang [1,2,*], Xiaoling Jian [1,2], Chao Wang [1,2] and Houjin Wang [1,2]

[1] Key Laboratory of Marine Mineral Resources, Ministry of Natural Resources, Guangzhou 511458, China; infiy@hotmail.com (X.Y.); jxiaoling@mail.cgs.gov.cn (X.J.); wchao@mail.cgs.gov.cn (C.W.); whoujin@mail.cgs.gov.cn (H.W.)

[2] Guangzhou Marine Geological Survey, China Geological Survey, Guangzhou 511458, China

* Correspondence: liujp980517@163.com (J.L.); gaiyun520@163.com (G.W.)

Abstract

The Lower Cretaceous fan-delta sandstones in the North Yellow Sea Basin underwent a distinctive polyphase burial trajectory, offering a natural laboratory to investigate path-dependent diagenesis and its impact on reservoir quality evolution in superimposed rift basins. Integrating petrographic, cathodoluminescence, SEM, and quantitative diagenetic analysis, this study reveals an anomalously compaction-dominated diagenetic regime wherein mechanical compaction accounted for 32.1% porosity loss (ICOMPACT ~0.8) compared to only 7.4% by cementation. This anomaly is attributed to a path-dependent mechanism as follows: a >60 Ma erosional hiatus arrested early calcite cementation, leaving sandstones mechanically metastable and vulnerable to intensified anomalous re-compaction triggered by rapid reburial since ~37 Ma during the Himalayan tectonic phase (since 66 Ma). The paragenetic sequence progresses from early poikilotopic calcite precipitation to late-stage microquartz, ferroan carbonates, and illitization, with intermediate feldspar dissolution generating secondary porosity. Critically, reservoir quality exhibits strong facies-dependent heterogeneity driven by divergent diagenetic pathways. Proximal matrix-supported gravels (Gcm/Gmm) are destroyed by pseudomatrix formation, whereas channelized sandstones (St/Sp) with localized early cement frameworks are buffered against compaction and preserve enhanced porosity (12%–18%) through subsequent dissolution. Consequently, this polyphase burial history fundamentally decouples reservoir quality from maximum burial depth. Effective reservoir prediction requires a paradigm shift from conventional depth-porosity transforms to integrated diagenetic facies analysis, validated by static petrophysical and well-log signatures (e.g., elevated Th/K ratios). These findings establish a transferable genetic model for evaluating porosity preservation in analogous Mesozoic polyphase-reactivated rift basins.

Keywords: path-dependent diagenesis; compaction-dominated diagenesis; fan-delta sandstones; reservoir quality; North Yellow Sea Basin

Check for updates

Academic Editor: Georgia Pe-Piper

Received: 2 June 2026
Revised: 2 August 2026
Accepted: 3 August 2026
Published: 4 August 2026

Copyright: © 2026 by the authors. Licensee MDPI, Basel, Switzerland. This article is an open access article distributed under the terms and conditions of the Creative Commons Attribution (CC BY) license.

1. Introduction

Sandstone reservoir quality is primarily controlled by the interplay of depositional facies and subsequent diagenetic alterations. Conventional burial-diagenesis models assume continuous burial and predict reservoir quality as a direct function of maximum depth and thermal maturity [1,2]. However, superimposed rift basins that have undergone

multiple tectonic inversions present a fundamentally different geological framework [2]. In these basins, the complexity of the burial history—characterized by uplift, erosion, and subsequent rapid reburial—decouples diagenetic evolution from present-day burial depth, posing significant challenges to conventional depth-porosity prediction models [3,4].

The North Yellow Sea Basin (location shown in Figure 1) is a Mesozoic-Cenozoic superimposed rift basin that experienced polyphase tectonism: Early Cretaceous rifting, Late Yanshanian uplift/erosion, and Himalayan rapid reburial [5–7]. Its Lower Cretaceous fan-delta sandstones (Figure 2) are prime exploration targets, yet recent drilling reveals highly heterogeneous porosity—tight sandstones at shallow depths juxtaposed with favorable reservoirs at greater depths, a pattern inconsistent with simple depth-porosity transforms [3].

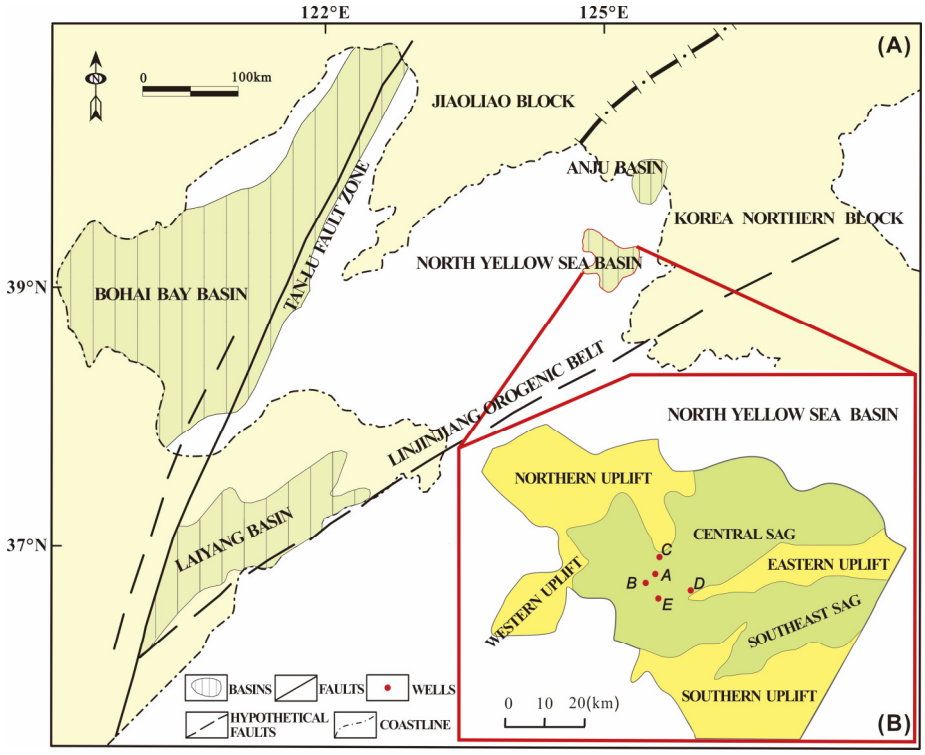


Figure 1. Location map of the North Yellow Sea Basin (**A**). Inset map shows the locality of the studied wells (**B**).

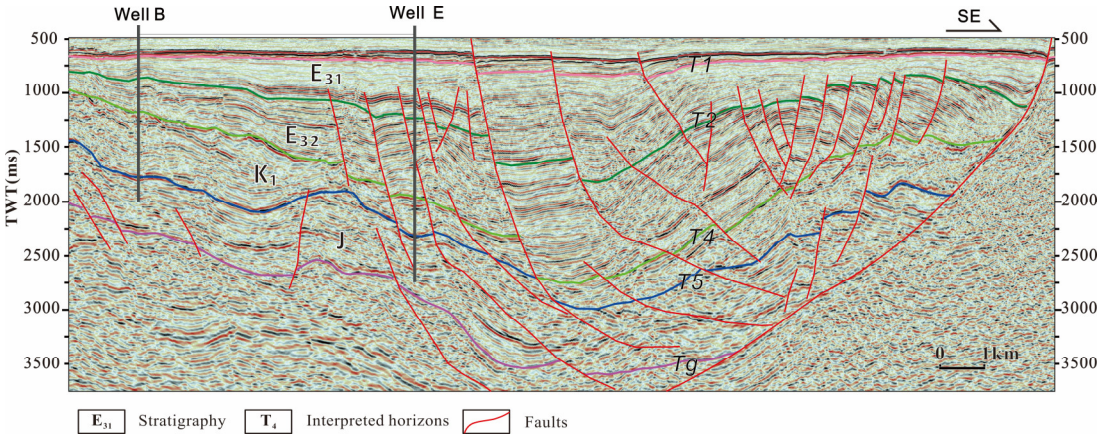


Figure 2. Representative 2D seismic cross section of the Lower Cretaceous sandstones.

A fundamental paradox exists in predicting reservoir quality in polyphase superimposed rift basins as follows: conventional depth-porosity transforms consistently fail, yet the mechanisms remain unclear. The central question is whether—and how—primary depositional architectures dictate divergent diagenetic pathways during reburial, decoupling reservoir quality from maximum burial depth. Facies-controlled diagenesis [2,3] offers the following theoretical foundation: depositional facies govern differential diagenetic responses. However, this concept has rarely been tested in basins that experienced prolonged hiatuses followed by rapid reburial—precisely where the depth-controlled paradigm most conspicuously fails [3]. We therefore test the hypothesis that depositional facies exert first-order control on compaction and subsequent diagenesis, using the Lower Cretaceous fan-delta sandstones of the North Yellow Sea Basin—a natural laboratory for polyphase reactivation—to establish a path-dependent diagenetic model.

To address these challenges, we integrate petrographic, mineralogical, and petrophysical data from six wells to (1) quantify the magnitude and mechanism of anomalous re-compaction driven by polyphase burial [1,4]; (2) establish the quantitative linkage between microfacies, diagenetic facies, and reservoir quality [8,9]; and (3) propose a diagenetic facies-based prediction framework validated by well-log signatures (e.g., Th/K ratios) for more robust subsurface risk assessment in superimposed rift basins.

2. Geological Setting

The Northern Yellow Sea Basin is a Mesozoic–Cenozoic continental rift basin developed atop the uplifted North China Platform [10–12]. Its basement comprises Archean–Proterozoic metamorphic rocks and Middle–Upper Paleozoic carbonate rocks and shales [13]. The basin fill includes, from bottom to top, Middle Jurassic, Upper Jurassic, Lower Cretaceous, Eocene, and Neogene–Quaternary strata [14,15].

The Lower Cretaceous succession—a predominantly red-colored, heterolithic clastic assemblage—represents the primary interval for favorable reservoir development [16]. The lower part consists of conglomerates, pebbly sandstones, coarse- to fine-grained sandstones, transitioning upward to reddish-brown mudstones interbedded with fine sandstones (Figure 3). Critically, the Lower Cretaceous experienced a distinctive polyphase burial trajectory as follows: slow burial from its base (~145 Ma) to ca.100 Ma during the early Yanshanian, followed by regional uplift and erosion during the late Yanshanian and early Himalayan tectonic phase (~100–37 Ma), and then rapid reburial since ~37 Ma during the Himalayan orogeny (66 Ma–present) [10,17–19]. The basal boundary of the Lower Cretaceous is currently buried at depths ranging from 1500 m to over 3000 m, indicating that the sediments have undergone significant consolidation [16,18].

A prolonged hiatus (~100–37 Ma) occurred after late Yanshanian uplift, during which the strata were partially to completely remove by erosion. Residual Lower Cretaceous thickness thus varies markedly across the basin, from 0 to 1750 m. The northwestern part preserves the thickest succession with more complete drilling intersections, whereas the southeastern part is thinned or locally absent due to erosion. Since the Oligocene, rapid and continuous accumulation of overlying strata has reburied the Lower Cretaceous to depths exceeding its pre-erosion burial depth, culminating in the present-day burial configuration. This polyphase burial history (early slow burial → uplift/erosion → rapid reburial) imposed a compound diagenetic regime on the Lower Cretaceous sandstones, making the basin an ideal natural laboratory to investigate how polyphase tectonic reactivation governs reservoir quality evolution.

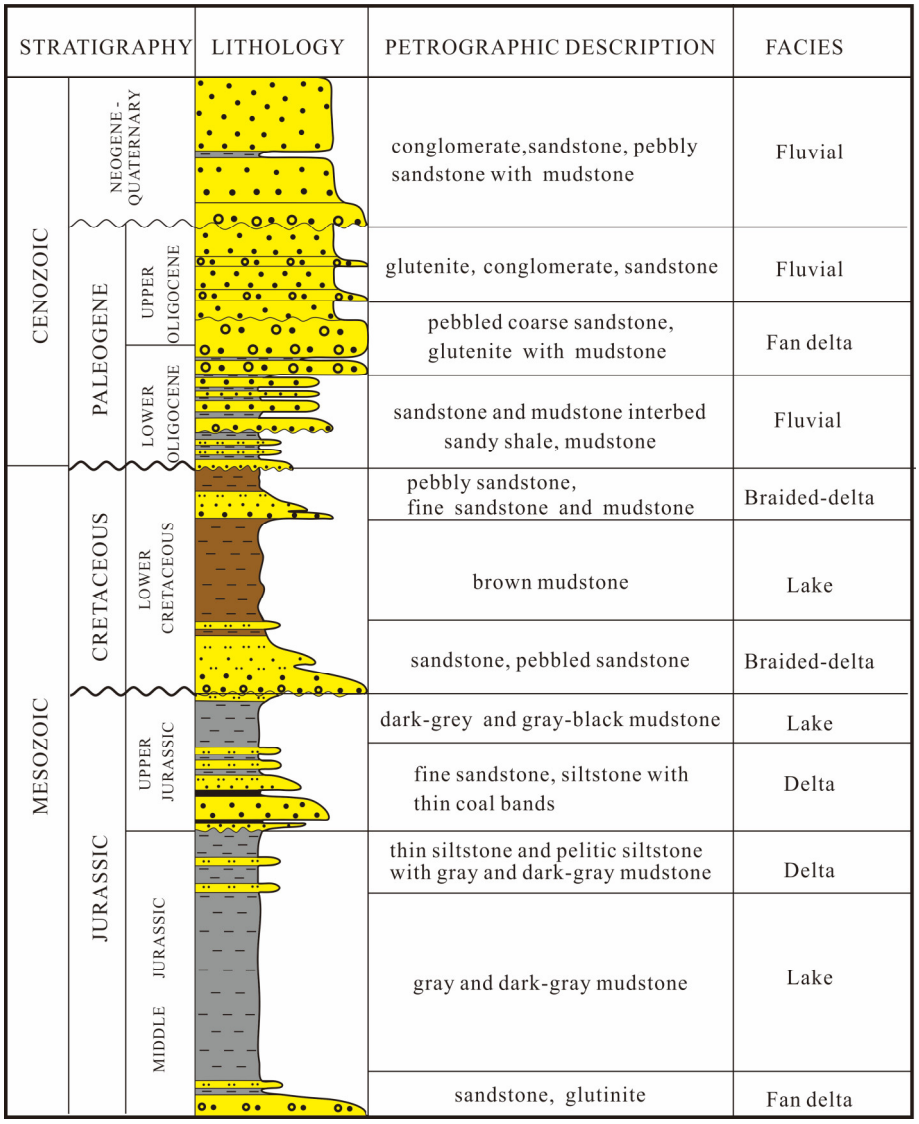


Figure 3. Generalized stratigraphy Mesozoic and Cenozoic sedimentary rocks of the North Yellow Sea Basin.

3. Materials and Methods

To investigate the diagenetic evolution and pore history of the Lower Cretaceous sandstones, this study integrated petrographic, petrophysical, and organic maturity data from six wells in the North Yellow Sea Basin.

3.1. Sample Collection

A total of 335 samples were collected from six wells. This includes 155 thin sections for petrography, 216 core plugs for petrophysical measurements, 85 samples for vitrinite reflectance, 16 for XRD, and 51 for elemental geochemical analysis (Th and K_2O).

3.2. Petrographic and Mineralogical Analyses

Modal compositions of 155 thin sections were determined using a Zeiss Axio Scope A1 polarizing microscope (Carl Zeiss AG, Oberkochen, Germany), following the Gazzi–Dickinson protocol [20] with 400 points per section. Reproducibility tests on 10% of sections (re-counted by a second operator) yielded < 5% relative error for major components. Cement and secondary porosity areas were quantified from digital photomicrographs using Image-Pro Plus V7.0.1 (Media Cybernetics), with ±2% analytical uncertainty. Bulk

mineralogy was obtained by XRD (Rigaku D/Max-2500 Rigaku Corporation, Akishima-shi, Tokyo, Japan, Cu Kα, 40 kV, 100 mA), with ~1% detection limit and ±2% uncertainty for major phases.

3.3. Cathodoluminescence (CL) and Scanning Electron Microscopy (SEM)

CL imaging was performed using a CAMBRIDGE CL8200 MK5 detector (Cambridge Image Technology Ltd. (CITL), Hatfield, United Kingdom) mounted on a Zeiss microscope, at 10 kV and 250 μA. SEM observations and EDS microanalyses were conducted on a Quanta200 instrument (FEI Company, Hillsboro, United States.), with analytical uncertainty < 0.5 wt% for major elements.

3.4. Quantitative Diagenetic Assessment

Quantitative porosity-loss evaluation followed the IGV framework [1], assuming an original porosity of 40% for the studied sandstones [21]. The calculations are as follows:

$$\mathrm{COPL} = 40\% - (\mathrm{IGV} - \mathrm{CEM})$$

$$\mathrm{CEPL} = \mathrm{CEM}$$

$$\mathrm{ICOMPACT} = \mathrm{COPL}/(\mathrm{COPL} + \mathrm{CEPL})$$

where IGV (bias-corrected per) is intergranular porosity plus cement, and CEM is intergranular cement volume. An ICOMPACT value > 0.5 indicates compaction-dominated porosity loss. Combined propagated uncertainties (from the original porosity assumption, point-counting statistics, and image estimation) are ±0.05 for ICOMPACT and ±3% for IGV.

To correlate porosity evolution with the polyphase burial history, total compaction ($\mathrm{COPL_{total}}$) was further deconvolved using early poikilotopic calcite (Calcite I) as an anchor. First-phase compaction ($\mathrm{COPL_1}$) is calculated as follows:

$$\mathrm{COPL_1} = 40\% - (\mathrm{IGV_{CalciteI}} - \mathrm{CEM_1})$$

where $\mathrm{IGV_{CalciteI}}$ is the intergranular volume preserved within early calcite frameworks, and $\mathrm{CEM_1}$ is early calcite volume. Second-phase compaction ($\mathrm{COPL_2}$), representing anomalous re-compaction during reburial, is derived by the following:

$$\mathrm{COPL_2} = \mathrm{COPL_{total}} - \mathrm{COPL_1}$$

Elastic rebound during the >60 Ma uplift is conservatively neglected, given the high ductile lithic content that primarily underwent irreversible plastic deformation.

3.5. Petrophysical and Thermal Maturity Measurements

Porosity was measured by helium porosimeter (uncertainty ± 0.3%) and permeability by gas permeameter (relative error < 5%). Th/K ratios were calculated from whole-rock Th (ppm) and $\mathrm{K_2O}$ (wt%) on 51 samples and paired with porosity measurements from the same depths. Thermal maturity was assessed via vitrinite reflectance on a DM4500P microscope with QDI302 microspectrophotometer (≥30 particles/sample; Ro uncertainty < ±0.05%). The burial history curve is adopted from the tectono-thermal model of Liu [18] for the North Yellow Sea Basin.

4. Results

4.1. Sedimentary Facies and Interpretations

Five lithofacies have been identified in the studied section of the Lower Cretaceous Sandstone (Figure 4). These include clast-supported gravels (Figure 4a,b), matrix-supported gravels (Figure 4c), cross-bedded sandstones (Figure 4d,e), parallel-laminated sandstone facies (Figure 4f,g), and silt/mudstones (Figure 4h). The facies classification follows the descriptive criteria of Liu et al. [22], Wang et al. [23], and Yu et al. [24]. Each facies is described below and summarized in Table 1. Collectively, these sedimentary units exhibit a series of generally upward-fining profiles.

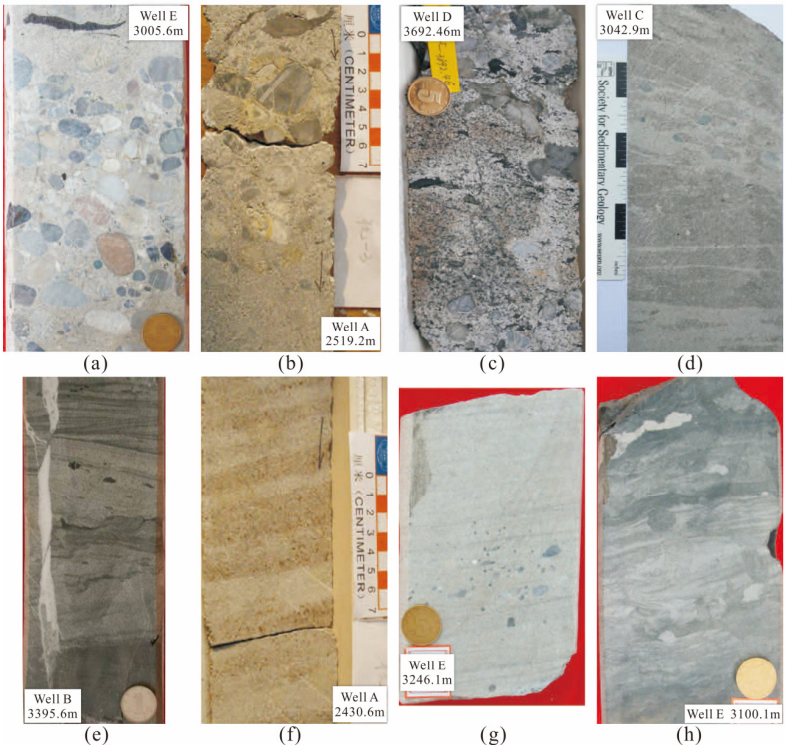


Figure 4. Photographs of sedimentary facies identified in the studied Lower Cretaceous sandstones. (**a**,**b**). Clast-supported massive gravel (Gcm); (**c**). matrix-supported gravel facies (Gmm); (**d**,**e**). cross-bedded sandstone facies (St); (**f**,**g**). parallel-bedded sandstones (Sp); (**h**). shale/mudstones (M).

Table 1. Classification, description, and interpretation of sedimentary facies for the studied Lower Cretaceous sandstones.

Facies Code	Description	Bed Thickness (cm)	Texture and Sedimentary Structures	Process	Interpretation
Gmm	Gravels with coarse-grained sandstone, gravels up to ~10 cm.	/	Massive; poorly sorted; sub-angular to sub-rounded grains; sharp to erosional contacts	High-energy flow	Channel lag deposits
Gcm	Angular to sub-angular clasts enclosed within a fine- to very coarse-grained sandstone matrix; with clay rip-up clasts	300	Massive; poorly sorted; poorly graded; no visible imbrication; erosional base	High-energy flow	Sheetflood deposits
St	Fine- to pebbly sandstone	10–20	Low-angle, staggered cross-stratification; moderately sorted	High-energy flow	In-channel and sinuous and bar deposits
Sp	Fine- to very coarse-grained sandstone, occasionally containing pebbles	5–60	Planar cross-lamination; moderately to well-sorted	Moderate-energy flow	In-channel migration of straight crested dunes
M	Gray, reddish-brown, and gray-brown mudstones with thin siltstone interbeds	1000–3500	Fine-grained	Low energy; suspension	Floodplain deposits

4.1.1. Clast-Supported Massive Gravel Facies (Gcm)

The clast-supported massive gravel facies is composed predominantly of gravels, with a minor component of fine- to very coarse-grained sandstone (Figure 4a,b). Grains are predominantly sub-angular to sub-rounded and poorly sorted. Gravel sizes range from pebble to cobble. The facies is mineralogically immature, containing feldspathic gravels up to approximately 10 cm in length that display a slightly preferred orientation. This facies occurs both as thin channel-lag deposits and as thick unstratified beds, with sharp to erosional contacts with overlying materials where present as discrete beds.

The mineralogically immature, poorly sorted, and poorly graded nature of these gravels suggests deposition by debris flows generated by inertial sediment transport or turbulence [25]. The transport of large clasts requires high-energy flow conditions capable of moving such coarse material downslope. These deposits likely record a rapid decrease in flow energy, possibly at the base of a slope. Alternatively, similar sediments may form during episodic seasonal rainfall events under sheetflood conditions.

4.1.2. Matrix-Supported Massive Gravel Facies (Gmm)

The matrix-supported conglomerate facies consist of angular to sub-angular, poorly sorted clasts ranging from pebble to cobble size, with no visible imbrication (Figure 4c). Clasts are enclosed within a matrix of fine- to very coarse-grained sandstone. The facies is poorly graded and occurs both as channel-lag fills and as thick beds of variable dimensions. A unit approximately 3 m thick is commonly associated with cross-bedded sandstones. Within amalgamated sand units, this facies often marks the onset of a new sedimentary cycle.

The erosional base and gravelly composition indicate deposition from viscous flows under high-energy hydrological conditions. Poor sorting and mineralogical immaturity suggest rapid deposition following a sharp energy decline close to the source area. Clay clasts associated with pebbly to coarse-grained sandstones are interpreted as rip-up clasts derived from channel erosion by high-energy flows. The massive to cross-bedded character of this facies is interpreted as sheetflood deposits [26].

4.1.3. Cross-Bedded Sandstone Facies (St)

The fine to pebbly sandstone is characterized by low-angle, staggered cross-stratification (Figure 4d,e). Grains are moderately sorted. Individual sets range from 10 cm to 20 cm in thickness, with cumulative thicknesses reaching approximately 2 m.

The cross-bedding is interpreted to have formed by the migration of three-dimensional dunes or megadunes within a fluvial channel [27]. Similar facies may also result from the migration of three-dimensional dunes or megaripples in coastal settings under the influence of longshore or tidal currents [28].

4.1.4. Parallel-Laminted Sandstone Facies (Sp))

This facies consists of fine- to very coarse-grained sandstone, occasionally containing pebbles (Figure 4f,g). It is typically moderately to well-sorted. Individual beds range from 5 to 60 cm in thickness, often forming units up to approximately 100 m thick. This facies is particularly common in the Lower Cretaceous core succession.

Parallel-laminated sandstone is interpreted as resulting from erosion on the upper surfaces of two-dimensional dunes and subsequent deposition of eroded material at flow-separation points. Under lower-flow regime conditions, sedimentation promotes the downstream migration of dunes within river channels [20]. Alternatively, such lamination may have formed in nearshore environments through the downstream migration of two-dimensional dunes or giant dunes [23].

4.1.5. Siltstone/Mudstone Facies (M)

This facies is characterized by gray, reddish-brown, and gray-brown mudstones with thin siltstone interbeds (Figure 4h). Bed thicknesses range from 10 to 35 m. These fine-grained deposits are commonly interbedded with cross-bedded sandstones (Figure 4h).

The facies is interpreted as suspension settling deposits in standing water bodies [29,30]. Similar facies have also been interpreted as overbank deposits on waterlogged floodplains or as ponded sediments in low-energy, shallow lacustrine environments.

4.2. Facies Associations

Based on high-resolution three-dimensional seismic data and genetically related lithofacies, Wang [16] and Yu [31] classified the Lower Cretaceous succession in the North Yellow Sea Basin into the following two distinct depositional systems: an aggradational fan delta system and a lacustrine system. These systems are characterized by recurring lithofacies assemblages that reflect distinct depositional processes and environmental settings.

The fan delta system is represented by assemblages of sedimentary conglomerates, cross-bedded sandstones, parallel-laminated sandstones, and large-scale, inclined-bedded sandstones. These facies associations are interpreted as channel and bar deposits formed under relatively high-energy conditions within an aggradational fan delta setting. The presence of erosional basal surfaces within these successions further supports the interpretation of active channel scour and subsequent infill, consistent with progradational fan delta processes [27,28].

In contrast, the lacustrine system is characterized by associations of reddish-brown, gray-brown, and gray mudstones, argillaceous siltstones, and interbedded mudstones with siltstones. These fine-grained lithofacies lack evidence of strong current activity and are interpreted as suspension settling deposits in a shallow lacustrine environment. The presence of reddish-brown to gray-brown coloration suggests periodic subaerial exposure and variable redox conditions, typical of low-energy, shallow lake settings with fluctuating water levels.

Together, these two depositional systems record a transition from proximal fan delta environments to more distal, lower-energy lacustrine settings, reflecting the interplay between sediment supply, basin subsidence, and paleogeographic configuration during the Early Cretaceous in the North Yellow Sea Basin.

4.3. Sandstones Composition and Texture

The Lower Cretaceous sandstones studied are medium- to extremely coarse-grained (Figure 5A), with grain sizes ranging from 0.57 mm to 5.15 mm (average 1.97 mm). The sandstones are poorly sorted, with sorting (standard deviation) values ranging from 0.36 mm to 0.88 mm (average 0.58 mm; Table 2). A plot of mean grain size versus sorting shows no significant positive or negative correlation (Figure 5B), a characteristic consistent with the grain-size statistical signature of fan delta sedimentary systems.

Following the classification scheme of Folk [32], the studied Lower Cretaceous sandstones are compositionally classified as feldspathic litharenites and lithic feldspathic sandstones (Figure 6). Detrital grains are predominantly sub-angular to sub-rounded. Petrographic observations indicate that quartz is the dominant detrital component, occurring as both monocrystalline and polycrystalline grains (the latter serving as metamorphic rock fragments), followed by clay minerals as the second most abundant fraction. Consistent with their feldspathic-lithic classification, potassium feldspar is more abundant than plagioclase, and rock fragments constitute a significant proportion. These rock fragments are primarily igneous in origin (including granite, tuff, and rhyolite), alongside mudstone lithic fragments that range from 15% to 55%, while heavy minerals are present merely as accessory phases. These detailed petrographic characteristics align well with the bulk

mineralogy summarized in Table 2, which also confirms the presence of plagioclase, albite, calcite, dolomite, siderite, anhydrite, and hematite in trace to minor amounts (generally a few percent).

Table 2. Bulk XRD data for the studied Lower Cretaceous Sandstones.

SN	Depth (m)	Q	Kf	Ab	Cal	Dol	Sd	Anh	Hm	Clay
A1	1260	57	10	4	trace	2	7	trace	trace	20
A2	1336.3	52	8	3	12	4	trace	trace	trace	21
A3	2223.5	53	22	4	2	1	trace	trace	trace	18
A4	2224.9	47	10	4	10	8	trace	trace	trace	21
A5	2226.9	61	4	5	11	6	trace	trace	trace	13
A6	2228.3	53	9	3	5	11	3	trace	trace	16
A7	2432	60	7	7	3	3	trace	trace	trace	20
A8	2436	67	6	5	3	trace	2	trace	trace	17
B1	1820.8	82	5	2	trace	trace	trace	2	trace	9
B2	1901.2	51	8	3	21	15	trace	trace	trace	2
B3	1987.9	61	11	1	7	13	trace	trace	trace	7
B4	2044.9	69	10	4	3	7	trace	trace	trace	7
B5	2093.5	79	6	trace	3	8	trace	1	trace	3
B6	2111.5	65	3	trace	8	12	trace	trace	1	11
B7	2210.6	74	10	trace	trace	5	trace	trace	trace	11
B8	2283	68	7	trace	7	6	trace	trace	trace	12
C1	830.9	59	26	12	trace	trace	trace	trace	trace	3
C2	1292.35	71	9	9	5	trace	trace	trace	1	5
C3	1501.75	51	17	13	trace	trace	trace	trace	trace	19
C4	1612.55	55	13	11	2	trace	trace	trace	1	18
C5	1665.5	79	3	1	trace	2	trace	trace	trace	15
C6	1762.5	61	20	12	1	trace	trace	trace	trace	6
C7	2256.8	58	17	7	2	4	trace	trace	trace	12
C8	2333.55	49	11	7	4	12	trace	trace	trace	17
C9	2334.65	52	3	8	5	10	3	trace	trace	19
C10	2381	56	5	trace	5	17	2	trace	trace	15
C11	2509.3	68	11	trace	2	2	trace	trace	trace	17
C12	2525.5	66	2	trace	14	4	trace	trace	trace	14
C13	2529	72	trace	trace	9	7	trace	trace	2	10
C14	2549.3	69	8	3	2	5	2	1	trace	10
C15	2550.6	55	9	2	7	1	2	1	trace	23
C16	2552.2	66	6	2	14	3	6	trace	trace	3
C17	2552.3	58	2	4	10	trace	trace	trace	trace	26
C18	2619	73	10	2	7	2	2	trace	trace	4
C19	2620.5	52	6	9	2	5	3	1	trace	22
C20	2624.4	67	11	6	2	2	8	trace	trace	4
C21	2643.5	70	2	trace	18	2	3	trace	trace	5
D1	1783.3	78	5	2	trace	6	trace	trace	trace	9
D2	2102.3	69	9	4	trace	7	trace	trace	trace	11
D3	2353.5	81	8	5	trace	trace	trace	trace	trace	6
D4	2656.1	70	2	2	13	5	trace	trace	trace	8
D5	2965.8	70	2	2	9	6	trace	trace	trace	11
D6	2967.2	52	9	3	3	8	trace	trace	trace	25
D7	2968.8	63	7	6	5	1	trace	trace	trace	18
D8	2969.3	58	7	2	8	2	trace	1	trace	22
D9	3049.75	60	3	1	12	2	trace	trace	trace	22
D10	3082.8	56	7	2	14	2	trace	trace	trace	19
D11	3083.7	58	11	5	2	9	trace	trace	trace	15
D12	3084.2	72	2	6	4	trace	1	trace	trace	15

SN = sample number; Clastic grains: Q = quartz; Kf = K-Feldspar; Ab = albite; Cal = calcite; Dol = dolomite; Sd = siderite; Anh = anhydrite; Hm = hematite.

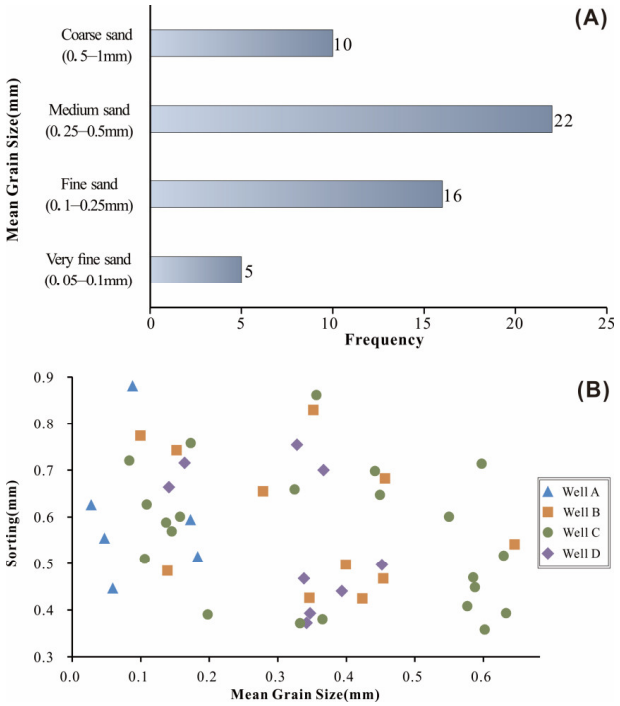


Figure 5. Textural characteristics of the studied Lower Cretaceous sandstones. (**A**) Relative proportion of grain size distribution showing the predominance of mediumgrained sandstones in the studied samples. (**B**) Plot of grain size against sorting showing a positive correlation.

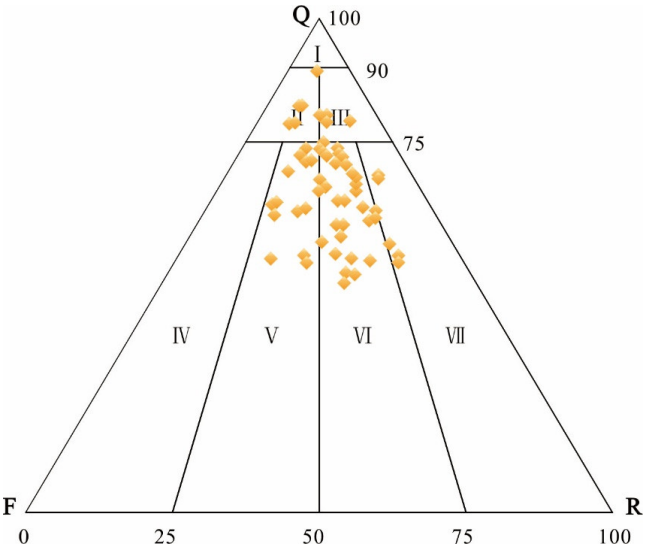


Figure 6. QFR plot showing the compositions of the studied Lower Cretaceous Sandstones.

4.4. Diagenetic Processes and Products

4.4.1. Mechanical Compaction

The Lower Cretaceous sandstones exhibit extensive evidence of mechanical and chemical compaction, which significantly reduced primary porosity (Figure 7). Petrographic analysis identifies the following three principal grain contacts types: (i) long contacts, where the longest sides of adjacent grains touch one another (Figure 7a,b); (ii) concavo-convex contacts, characterized by curved grain boundaries that typically involving the fracture of mechanically unstable grains (e.g., feldspar; Figure 7c); and (iii) sutured contacts, where grains have penetrated into one another, resulting in chemical dissolution of quartz at grain contacts and stylolite formation (Figure 7d). Microstructural observations indicate

that detrital grains slid past one another and became tightly packed during progressive burial, with all studied sandstones initially experiencing mechanical compaction prior to significant calcite cementation.

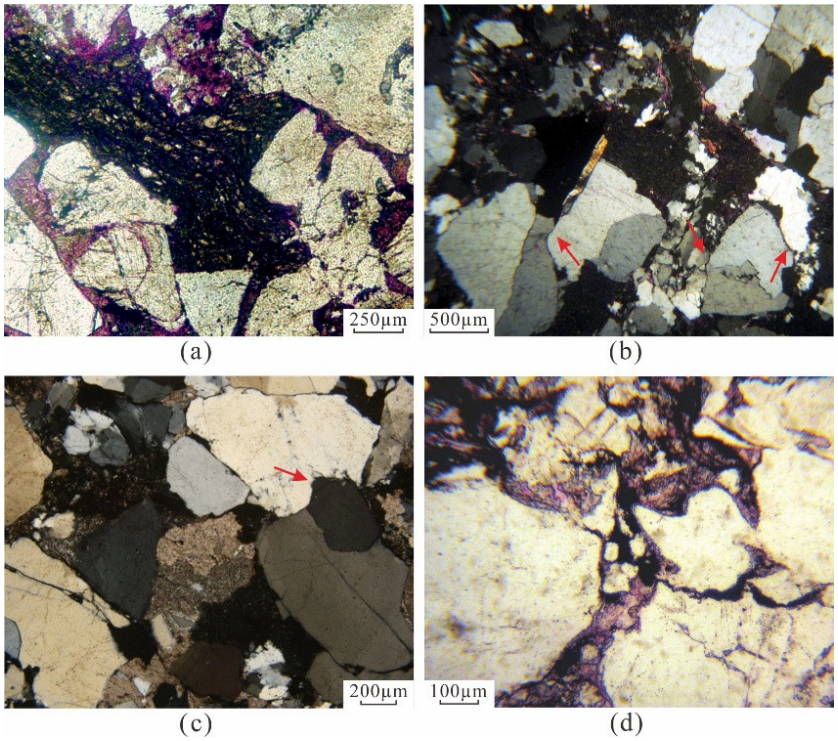


Figure 7. Types of grain contacts in the Lower Cretaceous sandstones. (**a**) Plastic deformation of fragment under mechanical compaction, single polars, NYS1, 2295.1 m; (**b**) concavo-convex contacts between quartz particles, cross polars, NYS3, 3095.2 m; (**c**) concavo-convex contacts between quartz particles, cross polars, NYS2, 2892.5 m; (**d**) sutured quartz particles, single polars, NYS3, 3091.55 m.

Assuming an original porosity of 40%, quantitative assessment using the IGV framework [1,21] demonstrates that intergranular porosity was predominantly reduced through compaction rather than cementation (Figure 8). Quantitatively, compactional porosity loss (COPL) ranges from 18.0% to 38.5% (average 32.1%), whereas cementational porosity loss (CEPL) ranges from 4.1% to 10.3% (average 7.4%). The calculated compaction index ranges from 0.8 to 0.9 (average 0.8), confirming a compaction-dominated diagenetic regime.

To quantitatively validate the path-dependent compaction mechanism, the total compactional porosity loss was deconvolved into two distinct burial phases using early poikilotopic calcite (Calcite I) as a volumetric anchor (detailed in Section 3.4). During the initial Yanshanian shallow burial (<1500 m), the intergranular volume preserved within early calcite frameworks (IGVCalcite I) averages ~35%, with early calcite cement (CEM_1) comprising ~4.0%. Consequently, the first-phase compactional porosity loss ($COPL_1$) is calculated to be 9.0%. In stark contrast, the second-phase compactional porosity loss ($COPL_2$), occurring during the rapid Himalayan reburial, reaches an average of 23.1%. This second-phase loss alone accounts for over 70% of the total porosity reduction and significantly exceeds the expected normal compaction loss for the corresponding increment of burial depth. This quantitative discrepancy confirms that the anomalous re-compaction was predominantly triggered and concentrated during the rapid Himalayan reburial phase.

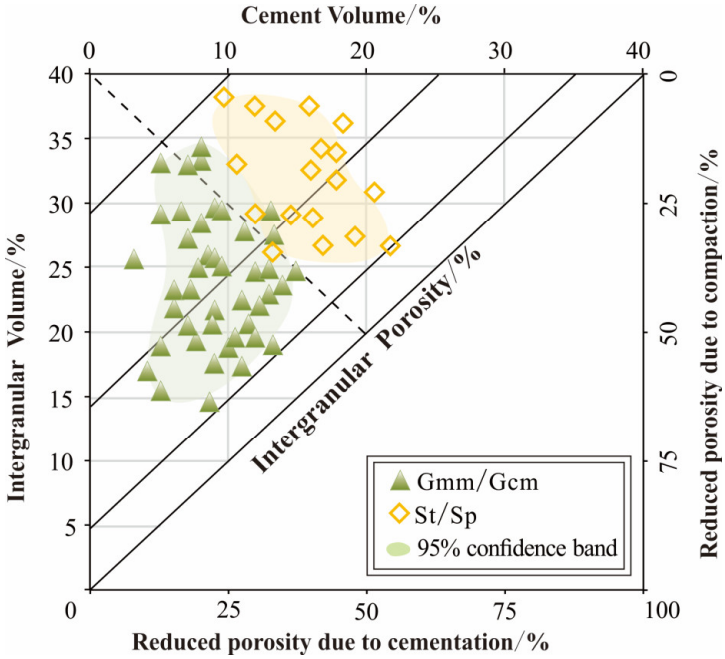


Figure 8. Plot of compactional porosity loss (COPL) against cementational porosity loss (CEPL) showing that compaction is the main driver for porosity loss in the Lower Cretaceous sandstones.

4.4.2. Characteristics of Carbonate Cements

Carbonate cement is the most abundant diagenetic phase in the studied sandstones, ranging from 3% to 15% (average 8.7%). The cement forms partial to complete coatings around detrital grains and locally replaces detrital components. Based on microscopic morphological observation and cathodoluminescence (CL) analysis, the following two generations of carbonate cement were identified: early-stage and late-stage.

Early-stage calcite cementation is characterized by in situ precipitation, often appearing as bright, euhedral crystal overgrowths [33]. Microstructural relationships reveal that these cements precipitated contemporaneously with early mechanical compaction, as evidenced by point contacts between detrital grains and undulatory extinction in framework grains [21,34,35]. Notably, basal calcite crystals were observed in the sandstones (Figure 9a), representing an early diagenetic product precipitated directly on detrital grain surfaces; in some instances, these early cements coalesce to form poikilotopic textures that engulf multiple detrital grains, a common feature in near-surface or shallow burial diagenetic environments [8].

During the late diagenetic stage, framework grains exhibit point-to-line or concavo-convex contacts, and authigenic calcite cements display three main occurrences. The first type predominantly fills feldspar dissolution pores, intergranular pores (Figure 9b), and grain microcracks (Figure 9c). The second type occurs as self-formed calcite crystals in the pores (Figure 9d), sometimes showing two phases of calcite enlargement with distinct growth zones visible under cross-polarized light (Figure 9e). The third type forms authigenic overgrowths on detrital calcite clasts (Figure 9g). The crosscutting relationships of these three occurrences indicate late-stage calcite cementation post-dated significant compaction [36,37].

Dolomite cement is generally low in abundance and occurs primarily as a replacement of calcite (Figure 9f). Thin-section observations reveal that dolomite commonly distributes along calcite crystal margins [1]. Furthermore, authigenic dolomite was found to replace clastic minerals and fill pores in certain samples (Figure 9h), indicating a late-stage diagenetic origin distinct from the calcite replacement process. Additionally, recrystallization

and enlargement phenomena of dolomite were observed in some samples (Figure 9i), suggesting textural modification during burial diagenesis [38].

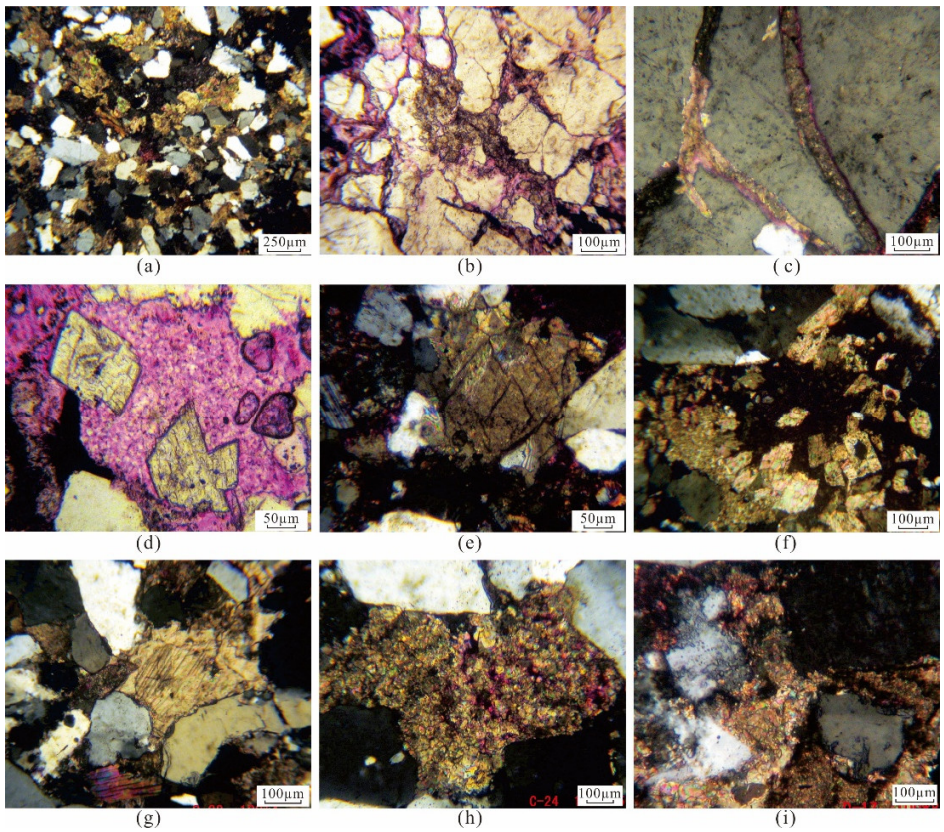


Figure 9. Mode of occurrence of calcite and dolomite in the Lower Cretaceous sandstones. (**a**) crystal basal calcite, cross-polarized, well D, 3477 m; (**b**) pore-filling calcite, plane-polarized, well B, 2956 m; (**c**) micro fracture filling calcite, plane-polarized, well D, 3049.75 m; (**d**) self-formed calcite crystals in pores, plane-polarized, well E, 3361 m; (**e**) two phases of calcite enlargements, cross-polarized, well B,2297.5 m; (**f**) calcite replacement by dolomite almost entirely, cross-polarized, well C, 2544.7 m; (**g**) authigenic enlargement of detrital calcite, cross-polarized, well C, 2340.95 m; (**h**) authigenic dolomite replaces clastic minerals and fills pores, cross-polarized, well E, 2337.40 m; (**i**) recrystallization and enlargement phenomenon of dolomite, cross-polarized, well D, 3044.80 m.

4.4.3. Characteristics of Quartz Cements

Quartz cements represent the second most abundant cement type in the Lower Cretaceous sandstones, predominantly composed of authigenic quartz overgrowths with minor amounts of microcrystalline quartz. As the most common form of quartz cement in many sandstone reservoirs [2], these overgrowths partially to completely encase detrital quartz grains, extending into the intergranular pore spaces and occluding primary porosity (Figure 10a). Petrographic observations indicate that their nucleation and growth are heavily dependent on the presence of grain-coating clays, precipitating primarily in areas where these coatings are absent, discontinuous, or poorly developed [3,39,40]. Within the sandstones, the interface between the detrital host grains and the overgrowths is typically delineated by dust rims or thin, discontinuous clay coatings (Figure 10a). In addition to overgrowths, microcrystalline quartz cement is also observed occurring directly between detrital quartz grains (Figure 10b), a texture often associated with advanced burial diagenesis [35,41].

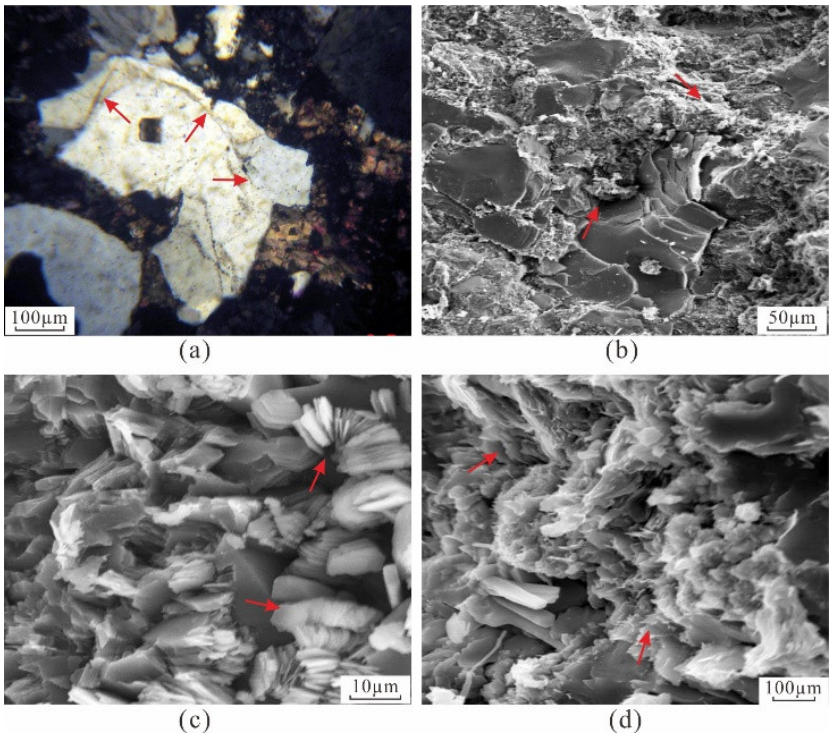


Figure 10. Development of quartz cements and clay minerals. (**a**) Blocky, well-developed quartz overgrowth around detrital quartz that reduces the intergranular pores, cross-polarized, well C, 2340.25 m; (**b**) microcrystalline quartz cement between detrital quartz grains, SEM, well A, 2932 m; (**c**) vermicular, booklet pore-filling kaolinite in intergranular pores and pore throats, SEM, well D, 2956 m; (**d**) flaky, fibrous pore-filling illite in intergranular pores and pore throats, SEM, well B, 2093.5 m.

4.4.4. Characteristics of Clay Cements

Clay minerals constitute another significant cement type in the studied sandstones, primarily consisting of illite, kaolinite, and minor chlorite. Petrographic and SEM observations reveal that the development of these authigenic clays is closely associated with feldspar dissolution. Partially dissolved K-feldspar grains not only generate secondary intragranular porosity but also act as a key material source for subsequent clay precipitation. Locally, this dissolution is accompanied by grain-replacive illite and some calcite. The dissolved components migrate into adjacent open intergranular pores and pore throats, where they precipitate as pore-filling kaolinite displaying characteristic vermicular and booklet morphologies (Figure 10c). Furthermore, illite extensively occupies the intergranular pores and pore throats as a pore-filling cement, exhibiting distinct flaky and fibrous morphologies under SEM (Figure 10d).

4.4.5. Mineral Dissolution and Replacement

Mineral dissolution in the study area primarily affects feldspar and calcite. Feldspar dissolution is prominently characterized by intense dissolution along cleavage planes (Figure 11a), as well as the development of intragranular fractures and dissolution pits. Furthermore, the dissolution of detrital feldspar grains generates secondary intergranular pores and fractures (Figure 11b), representing a significant mechanism for secondary porosity creation in clastic reservoirs [42]. Although the precise transport pathways of the dissolved products are complex, petrographic observations confirm that a portion of the material precipitated in situ. This localized reprecipitation led to variable degrees of kaolinization and the local formation of vermicular kaolinite aggregates, reflecting a coupled dissolution-precipitation process. Calcite dissolution affects both calcite cements

and detrital grains. SEM observations reveal that altered calcite grains lose their original well-crystallized surfaces, developing distinct vuggy porosity characterized by irregular dissolution pits and cavities (Figure 11c). Linear dissolution pits are also locally present, likely propagating along specific crystallographic directions.

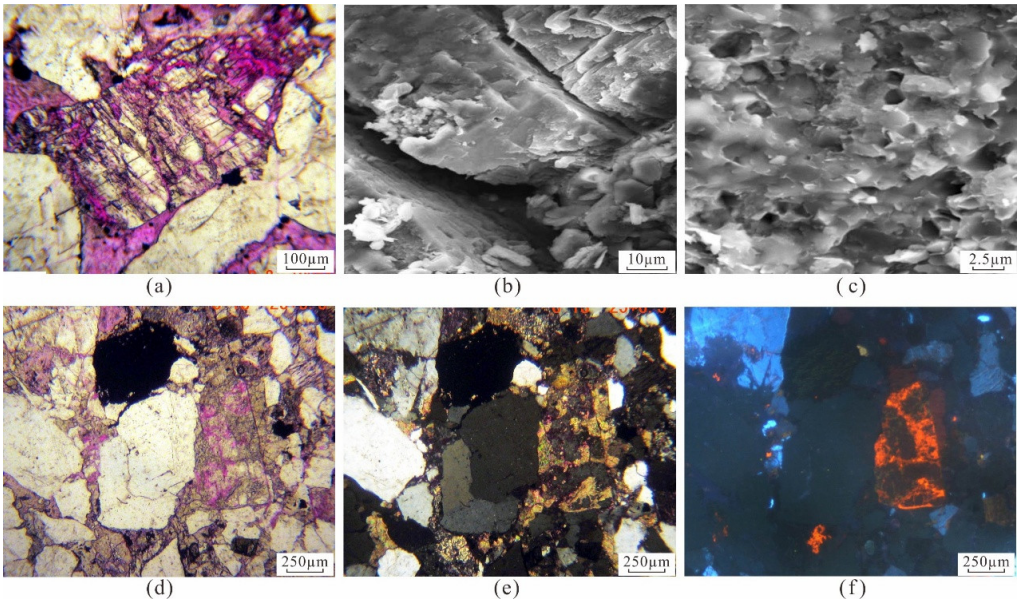


Figure 11. Alteration of debris particles. (**a**) Intensely dissolved feldspar along cleavage planes, plane-polarized, well A, 2295.1 m; (**b**) intergranular pores and fractures resulting from detrital feldspar dissolution, SEM, well E, 2339.85 m; (**c**) altered calcite grain, with vuggy pores developing on the surface, SEM, well B, 2340.9 m; (**d**–**f**) calcite replacement of feldspar observed under plane-polarized light (**d**), cross-polarized light (**e**) and cathodoluminescence (**f**). The feldspar grain retains its original shape despite the destruction of its internal structure, well C, 2416.86 m.

Metasomatism is a key diagenetic process in the Lower Cretaceous succession [14], notably involving the widespread replacement of feldspar by carbonate minerals [18]. Figure 11d–f illustrates a typical example of feldspar replacement by calcite observed under plane-polarized light, cross-polarized light, and CL. Although the internal structure of the feldspar grain has been completely destroyed and locally dissolved, it retains its original external shape. Under plane-polarized light, the dissolved portions are indicated by purple casting dye (Figure 11d). Under cross-polarized light, these areas exhibit the optical characteristics of carbonate minerals (Figure 11e). Under CL, the grain interior displays a distinct orange-red luminescence, a typical feature of calcite, confirming deep-seated alteration while preserving the original grain outline (Figure 11f). This textural preservation is characteristic of volumetrically constrained replacement reactions during burial diagenesis [3].

5. Discussion

5.1. Anomalous Re-Compaction: A Path-Dependent Genetic Mechanism

5.1.1. Discrimination of Anomalous Re-Compaction

Quantitative assessment reveals a compaction-dominated regime (COPL = 32.1%, CEPL = 7.4%, ICOMPACT = 0.81) that is atypical for ~3000 m burial. At equivalent depths, cementation-dominated regimes normally prevail (ICOMPACT < 0.5) [40], and the studied values even exceed those of lithic-rich basins such as the North Sea (~0.65) [3]. Petrographically, this anomaly is expressed by ubiquitous concavo-convex and sutured grain contacts (Figure 7b–d)—textures normally associated with >4000–5000 m burial. At

the present burial depth of ~3500 m and moderate thermal maturity (Ro = 1.1%–1.35%), such intense compaction is inconsistent with the <20% porosity loss expected from normal depth-dependent trends [40]. This systematic mismatch between shallow burial and deep-burial textures defines what we term anomalous re-compaction.

This path-dependent evolution is quantitatively anchored to the polyphase burial history modeled by Liu [18] (Figure 12), establishing a direct correspondence between porosity reduction and burial trajectory. During the first stage (Early Cretaceous syn-rift slow burial), the calculated first-phase compactional loss ($COPL_1$ = 9.0%) aligns with the gentle subsidence slope of the burial curve, representing normal mechanical compaction under shallow conditions. In the second stage (>60 Ma Yanshanian uplift and erosion), the burial curve exhibits a sharp inflection; diagenesis was effectively frozen, and porosity evolution stagnated, with minor elastic rebound conservatively neglected due to irreversible plastic deformation. Critically, in the third stage (rapid Himalayan reburial), the burial curve steepens dramatically. The second-phase compactional loss ($COPL_2$ = 23.1%) corresponds precisely to this steep segment, indicating that over 70% of the total porosity destruction was concentrated in this single episode. The rapid loading rate outpaced fluid pressure equilibration, directly translating the steep burial trajectory into the anomalously high $COPL_2$ and validating that anomalous re-compaction is a mechanically forced response to rapid reburial.

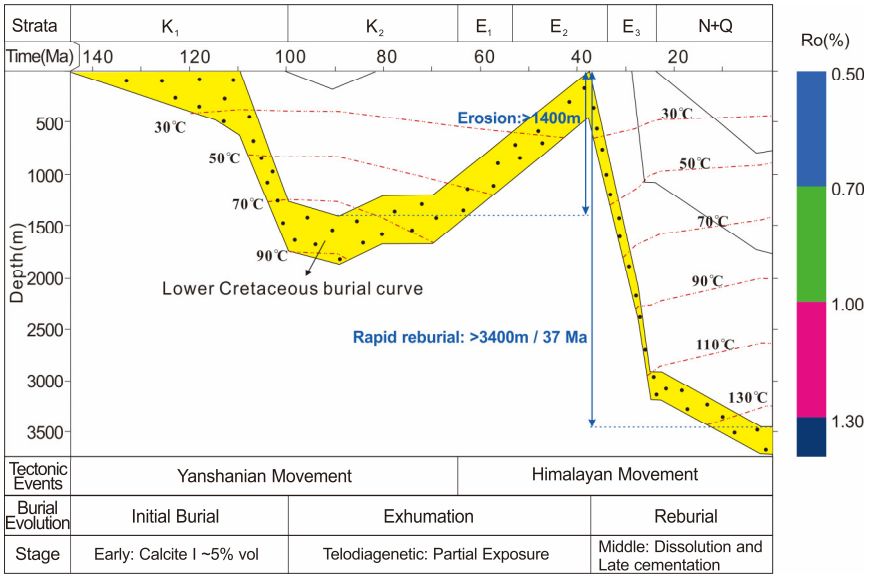


Figure 12. Representative burial history of Lower Cretaceous sandstones in Well D (modified from [18]).

To elucidate its origin, the compaction history is discriminated into the following three stages: predating compaction (Early Cretaceous syn-rift shallow burial), a frozen re-compaction stage (>60 Ma Yanshanian uplift/erosion), and anomalous re-compaction (rapid Himalayan reburial). This path-dependent evolution is quantitatively anchored to the polyphase burial history modeled by Liu [18] (Figure 12). The first-phase loss ($COPL_1$ = 9.0%) aligns with the gentle syn-rift subsidence slope, whereas the second-phase loss ($COPL_2$ = 23.1%) corresponds precisely to the steep Himalayan reburial segment, accounting for >70% of total porosity destruction. The rapid loading rate outpaced fluid-pressure equilibration, translating the steep burial trajectory directly into an anomalously high $COPL_2$ and confirming that anomalous re-compaction is a mechanically forced response to rapid reburial.

5.1.2. Quantitative Constraints on Compaction History

The predating compaction stage is characterized by shallow burial (<1500 m), point-contact fabrics, and patchy early poikilotopic calcite (Calcite I) (Figure 7b,c). Slow burial limited chemical diagenesis, resulting in discontinuous cement frameworks rather than pervasive rigid supports. Although substantial residual porosity was retained, the sandstones existed in a mechanically weak state prior to the Late Yanshanian uplift.

This uplift imposed a >60 Ma erosional hiatus, during which up to 1400 m of strata were removed in the basin center [18]. Diagenesis was effectively frozen before framework-stabilizing cements could develop. Consequently, the sandstones re-entered the burial realm in a mechanically metastable state—lacking rigid carbonate frameworks yet not possessing unconsolidated porosity. This metastability is the prerequisite for the subsequent departure from conventional re-compaction.

5.1.3. Genetic Mechanism: Path-Dependent Evolution

This polyphase trajectory is independently corroborated by vitrinite reflectance data. Measured Ro values (0.77%–1.35%) track the modeled temperature-time path in Figure 12: Early Cretaceous syn-rift subsidence elevated Ro to ~0.7%–0.9% within the 70–90 °C window; the >60 Ma Yanshanian hiatus froze maturation at these peak paleotemperatures; and Himalayan reburial raised Ro to the present 1.1%–1.35% range within the 130–150 °C window. The consistency between measured Ro and the temperature–time paths independently confirms that the diagenetic state records integrated thermal exposure across multiple burial episodes, rather than simply the present ~3000 m depth.

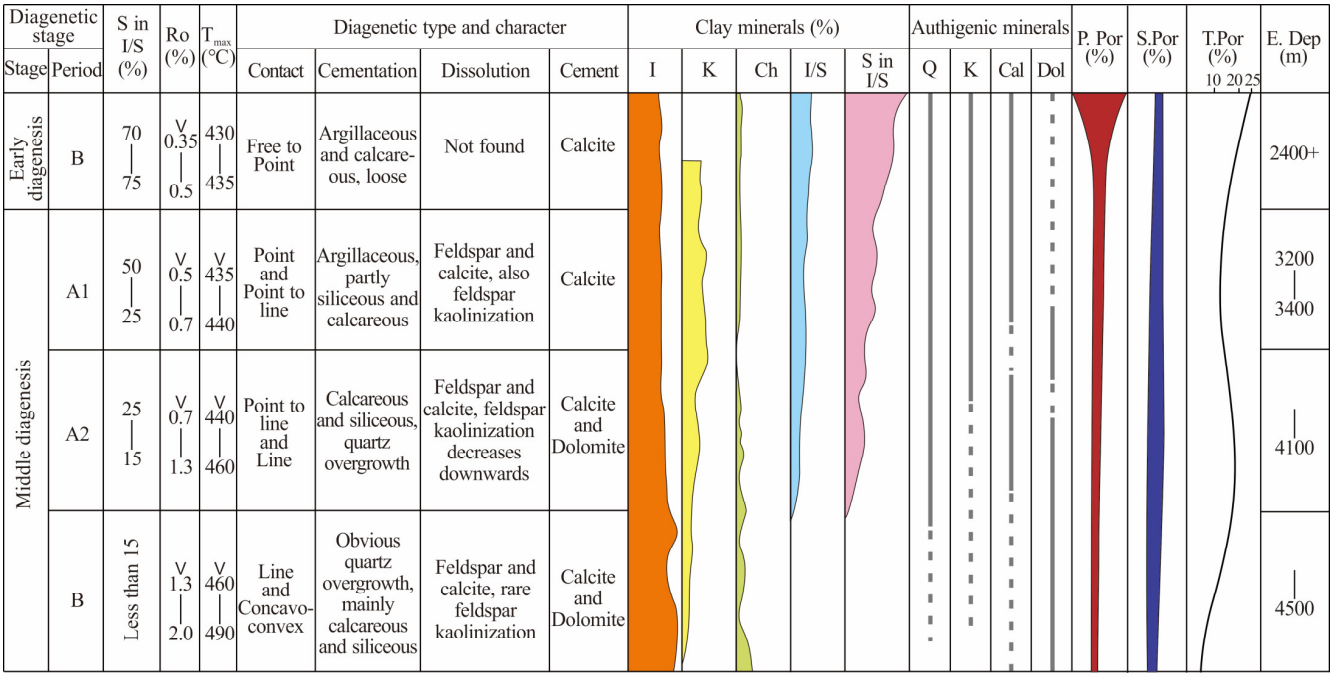
Upon Himalayan reburial (ca. 37 Ma; Figure 12), the thermally mature but mechanically metastable reservoir experienced abrupt stress intensification. Rapid sedimentation outpaced fluid-pressure equilibration, preventing the establishment of a rigid load-bearing framework. Rather than following normal compaction curves, these sandstones underwent anomalous re-compaction, manifested by COPL > 30% and pervasive concavo-convex/sutured contacts (Figure 7b–d)—features typical of much greater depths. This path-dependent behavior stems from a pre-conditioning effect: early burial induced irreversible grain rearrangement, and prolonged uplift generated micro fractures. During rapid Himalayan reburial, these pre-existing flaws acted as stress concentrators. With anomalously high effective stresses acting directly on the incompletely cemented frameworks, mechanical compaction and pressure solution were rapidly reactivated, driving maximum porosity reduction.

The textural and compositional immaturity of the fan-delta sandstones further exacerbated this susceptibility. High proportions of ductile lithic fragments (15%–48%; Table 2) and poor sorting provided abundant sites for stress concentration [34]. Critically, the absence of pervasive early carbonate frameworks—due to interruption by the Yanshanian uplift—deprived the sandstones of rigid skeletal support, leaving intervening sandstone beds vulnerable to intensified anomalous re-compaction. The facies-specific manifestation of this mechanism is detailed in Section 5.3.

5.2. Paragenetic Sequence and Fluid Evolution

The sequence commenced with early mechanical compaction and the precipitation of poikilotopic calcite (Calcite I) during the initial Yanshanian burial (Figure 13). As shown in Figure 9a, Calcite I exhibits bright orange-yellow luminescence under CL, a signature of low-iron, manganese-activated calcite precipitated from oxidizing, shallow-burial fluids (e.g., meteoric or connate waters). These cements display poikilotopic textures, engulfing detrital grains with curved crystal boundaries that conform to particle outlines, and are associated with point-contact grain fabrics—consistent with precipitation contemporane-

ous with initial mechanical compaction (Figure 13). The shallow burial depth (typically <1500 m during the initial Yanshanian subsidence) and low Ro values (0.35–0.5%) further confirm an early diagenetic environment dominated by oxidizing conditions.



Note:In the authigenic minerals column of the figure, Q = quartz overgrowth, K = kaolinite, cal = authigenic calcite, dol = authigenic dolomite. P.Por=Primary porosity(%), S.por=Secondary porosity(%), T.por=Total porosity(%), E.dep=Equivalent depth(m).

Figure 13. Paragenetic sequence of diagenetic events for the Lower Cretaceous sandstones. In the authigenic minerals column, Q = quartz overgrowth, K = authigenic. kaolinite, Cal = authigenic calcite, Dol = authigenic dolomite. P.Por = primary porosity (%), S.Por = secondary porosity (%), T.Por = total porosity (%), E.Dep = equivalent depth (m).

The subsequent Himalayan reburial triggered a second generation of cementation, characterized by microcrystalline quartz, late-stage calcite (Calcite II), and ferroan dolomite (Figure 13). Calcite II and associated dolomite exhibit dull orange to non-luminescent CL signatures, indicative of ferroan compositions and reducing conditions (Figure 9f). Microcrystalline quartz, abundant in intergranular pores (Figure 10a, b), likely precipitated from silica released during the smectite-to-illite transformation, a process intensified during rapid Himalayan burial [19,33]. The increase in Ro values (0.7%–1.35%) and decrease in I/S ratio (from 70% to 75% to <15%, Figure 13) confirm an advanced diagenetic stage.

The anomalously high Ro values (up to 1.35%) relative to the moderate maximum physical burial depth (~3000 m) likely reflect the cumulative thermal effects of the polyphase burial history, validating that diagenetic progression is controlled by integrated thermal exposure rather than monotonically increasing physical depth.

Secondary porosity generation, primarily through feldspar dissolution and selective calcite removal, represents the final major diagenetic modification (Figure 11). This timing suggests dissolution occurred during the transition from early to late diagenesis (Figure 13), potentially coinciding with the influx of organic acids from source rock maturation [42]. The absence of extensive meteoric dissolution features indicates leaching was driven by internal fluid-buffer reactions (Figure 13). Consequently, the secondary porosity system represents a closed-system dissolution event, where alteration products (kaolinite, silica) were locally reprecipitated as authigenic cements, resulting in limited net porosity gain [43,44]. Overall, the paragenetic sequence documented in Figure 13 provides a coherent temporal framework, confirming that polyphase burial evolution fundamentally

controls diagenetic processes and fluid chemistry shifts from oxidizing to reducing conditions in this superimposed basin.

5.3. Facies-Dependent Diagenetic Heterogeneity

While the anomalous re-compaction mechanism (Section 5.1) applies basin-wide, the highly heterogeneous spatial distribution of reservoir quality fundamentally reflects how primary depositional architecture dictate divergent diagenetic pathways during re-compaction [8]. The concept of diagenetic facies—genetically related packages of sedimentary rocks that experienced similar diagenetic pathways due to shared compositional and textural attributes—provides a critical framework for resolving this heterogeneity [45]. In the North Yellow Sea Basin, the rapid lateral facies transitions characteristic of aggradational fan-delta environments created distinct petrophysical domains that responded differentially to the anomalous re-compaction triggered by Himalayan rapid reburial. Consequently, heterogeneity in this superimposed basin is primarily controlled by facies-dependent diagenetic susceptibility, which decouples reservoir quality from uniform burial depth trends.

This facies control is most pronounced along the sedimentary transport path. Proximal matrix-supported and clast-supported massive gravel deposits (Gmm/Gcm; Figure 4a–c) exhibit the poorest reservoir quality. In the COPL-CEPL plot (Figure 8), Gmm/Gcm samples cluster in the upper-left quadrant (COPL > 35%, CEPL < 5%), representing a compaction-dominated domain. This is a direct consequence of inherent textural immaturity: bimodal grain-size distributions and high matrix content (up to 40%) created abundant stress concentration sites. Under Himalayan reburial, these ductile components underwent pervasive pseudomatrix formation, obliterating primary porosity [34]. Furthermore, the muddy matrix inhibited the development of a continuous, rigid early calcite cement framework (Calcite I), leaving the sediments highly vulnerable to anomalous re-compaction. The resulting "compaction-dominated, matrix-rich" diagenetic facies exhibits negligible intergranular porosity (<3%) and permeabilities typically below 0.1 mD, rendering these intervals non-reservoir units.

Conversely, fan-delta front and distributary channels architectural elements—represented by cross-bedded (St) and parallel-laminated (Sp) sandstones (Figure 4d–g)—constitute the "sweet spots". St/Sp samples exhibit a divergent trajectory in Figure 8, spreading across the moderate-COPL and relatively higher-CEPL domain (ICOMPACT 0.75–0.85). These moderately sorted, medium- to coarse-grained sandstones initially possessed stable grain fabrics. Their relatively clean, matrix-poor texture allowed the development of patchy but locally rigid early calcite frameworks that buffered against complete compaction during Yanshanian burial. Subsequently, the high detrital feldspar content (15%–25%) provided reactive substrates for dissolution during the late diagenesis, generating significant secondary porosity (Figures 10 and 11). Although secondary porosity formation was constrained by closed-system conditions (Section 5.2), its superimposition upon preserved primary porosity yields a relative improvement compared to adjacent, non-dissolved lithofacies. This "cementation-buffered, dissolution-enhanced" diagenetic facies yields anomalously high total porosities of 12%–18% and permeabilities exceeding 10 mD, serving as efficient carrier beds for hydrocarbon migration [46,47].

Despite a uniform feldspathic litharenite composition (Figure 6), distinct compaction-cementation pathways appear in Figure 8. This divergence indicates that depositional facies—specifically textural attributes like sorting and matrix content—are the primary controls on mechanical response. For instance, even St/Sp samples with high ductile lithic content show only marginally elevated COPL compared to cleaner intervals, a stark contrast to the intense deformation in the matrix-supported Gmm/Gcm facies. Thus, while

lithology acts as a secondary reinforcing factor, the depositional architecture fundamentally governs stress distribution and cementation potential.

Beyond coarse-grained facies, the fine-grained prodelta and shallow lacustrine mudstones (M facies; Figure 4g,h) function as stratigraphic elements modifying fluid flow. Characterized by high clay content (>60%), abundant iron oxides, these units underwent rapid early lithification, serving as vertical flow barriers during prolonged burial. They compartmentalized the reservoir into discrete hydrological cells and created local overpressure compartments during rapid Himalayan burial, potentially preserving porosity in adjacent sandstones through mechanical unloading. Thus, the M facies acts as a "protective diagenetic envelope".

Integrating these responses permits the delineation of three distinct diagenetic facies associations (Table 3) as a predictive template as follows: Diagenetic Facies I (matrix-rich compactional, Gmm/Gcm), Diagenetic Facies II (cementation-buffered dissolutional, St/Sp), and Diagenetic Facies III (protective diagenetic envelope, M facies). This model dictates that exploration efforts should focus on the mid-fan to outer-fan transition zones where Diagenetic Facies II attains maximum thickness and is adequately sealed by Diagenetic Facies III, while explicitly avoiding the basin-margin proximal areas dominated by Diagenetic Facies I.

Table 3. Predictive template of diagenetic facies associations for reservoir quality and exploration targeting the Lower Cretaceous fan-delta sandstones.

NO.	Diagenetic Facies Association	Corresponding Lithofacies and Spatial Setting	Key Petrophysical and Diagenetic Parameters	Reservoir Quality and Exploration Implications
I	Compaction dominated, matrix-rich	Gmm, Gcm facies; Basin-margin proximal areas	ICOMPACT > 0.85; total ϕ < 3%; K < 0.1 mD	Non-reservoir. Should be explicitly avoided as drilling targets regardless of burial depth.
II	Cementation-buffered, dissolution-enhanced	St, Sp facies; Mid-fan to outer-fan transition zones	ICOMPACT 0.75–0.85; secondary ϕ > 5% (up to 8%–12%); total ϕ 12%–18%; K > 10 mD	Primary reservoir target. Particularly viable where facies stack vertically to form amalgamated channel complexes > 5 m.
III	Protective diagenetic envelope (mudstone seal)	M facies; distal prodelta to shallow lacustrine	Thickness: 10–35 m; very low permeability	No intrinsic reservoir value but defines top-seal integrity and lateral compartmentalization for Facies II.

5.4. Implications for Reservoir Quality Prediction and Hydrocarbon Exploration

The diagenetic investigation of the Lower Cretaceous sandstones fundamentally reframes the exploration risk model for the North Yellow Sea Basin, shifting the primary uncertainty from "depth-dependent porosity decay" to "path-dependent diagenetic overprint." Conventional exploration screening in rift basins typically employs simple depth-porosity transforms to predict reservoir quality, assuming continuous burial and uniform lithology. However, this study demonstrates that the Yanshanian–Himalayan polyphase burial decouples reservoir quality from maximum burial depth. The validity of this diagenetic heterogeneity model is independently confirmed by the strong correlation between static well-log signatures and measured petrophysical properties. Consequently, the critical exploration risks shift to facies misidentification and burial pathway miscalculation.

To operationalize the diagenetic facies framework established in Table 3 for subsurface prediction, specific well-log and seismic criteria must be applied. In terms of depositional architecture, high-resolution seismic geomorphology can distinguish favorable amalgamated channel complexes (St/Sp facies) from chaotic debris-flow deposits (Gmm/Gcm) [48]. Well-log responses provide critical insights into diagenetic overprints. Intervals with patchy early calcite cementation (Calcite I) that buffered compaction typically exhibit elevated sonic transit times (>280 μs/m) and moderate resistivity (5–20 Ω·m), contrasting with high-resistivity tight zones (>50 Ω·m) characterized by pervasive late-stage cementation. Furthermore, feldspar dissolution zones exhibit elevated thorium/potassium (Th/K) ratios

from gamma-ray spectroscopy, driven by the relative enrichment of radioactive thorium versus potassium-bearing feldspars during alteration, which serves as a diagnostic indicator of secondary porosity development [49]. The neutron-density cross-plot separation (φN > φD) further corroborates the presence of these dissolution-enhanced intervals.

To quantitatively validate the Th/K ratio as a well-log proxy for dissolution-enhanced porosity, we cross-plotted Th/K against core-measured porosity for 51 paired samples (Figure 14). A logarithmic regression yields a statistically significant positive correlation ($R^2 = 0.33$, $p < 0.01$). St/Sp samples systematically occupy the high-Th/K domain (>4.0) with elevated porosity (mean 10.2%), whereas Gmm/Gcm samples cluster at Th/K < 6 with porosity consistently below 10.4% (mean 6.2%; *t*-test, $p < 0.001$). This facies-based separation confirms that a Th/K threshold of ~4.0 effectively discriminates the dissolution-enhanced diagenetic facies (Diagenetic Facies II) from compaction-dominated intervals, providing a readily implementable criterion for screening favorable reservoir zones in the absence of core data. While dynamic production data are not yet available for these recent exploration wells, the strong correlation between the predicted diagenetic facies (Table 3) and static petrophysical properties (Figure 14) provides a robust basis for future flow-unit modeling and production forecasting.

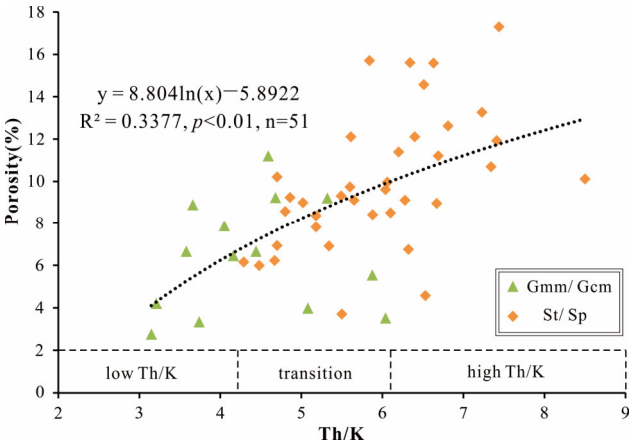


Figure 14. ThK vs. core porosity cross-plot (differentiated by facies; logarithmic fit).

The spatial and depth distribution of these diagnostic signatures reveals an optimal "reactivation window" (approximately 1500–2200 m present depth) where early cement frameworks buffered compaction and secondary porosity remains unoccluded by late cements. Although favorable channel facies locally persist in deeper intervals (>2200 m), these zones face a progressively higher risk of pervasive late-stage quartz and ferroan carbonate occlusion. This diagenetic constraint necessitates differentiated exploration strategies. In the northwestern thick-bedded zone (residual thickness > 1000 m), exploration should target stacked channel systems. Conversely, the southeastern thin-skinned zone (residual thickness < 500 m) presents high risks due to intense late compaction near the erosion limit, evidenced by dry tests in wells penetrating compaction-dominated Diagenetic Facies I at shallow depths. Thus, this region should be deprioritized unless exceptional Early Cretaceous paleo-highs with early cementation are identified.

These findings establish a transferable genetic model for evaluating porosity preservation in analogous Mesozoic polyphase-reactivated rift basins along the east Asian continental margin. When compared with similar tectonic settings, such as the Bohai Bay Basin (polyphase rifting) or the North Sea Basin (tectonic inversion), the following three universal discriminants emerge for reservoir prediction in superimposed basins: (1) a significant erosional hiatus (>60 Ma) typically inhibits the development of rigid early carbonate ce-

ments, predisposing the reservoir to anomalous re-compaction risks during subsequent rapid reburial; (2) within fan-delta systems, channel microfacies (St/Sp) consistently acts as compaction-resistant "sweet spots" due to localized early cementation buffers; and (3) well-log Th/K ratios and sonic transit times serve as universal geophysical indicators for identifying these dissolution-enhanced zones, offering a robust tool for reducing exploration uncertainty in structurally complex basins.

Despite the robust diagenetic framework presented herein, several limitations constrain predictive certainty and warrant targeted future investigation. (1) Data Spatiotemporal Gaps: The current dataset is biased toward the northwestern depocenter, lacking core control in the southeastern erosional zone or intermediate burial-depth intervals (500–1000 m), limiting validation of the re-compaction model across the full burial spectrum. (2) Thermal Calibration: The absence of fluid inclusion microthermometry and precise (U-Th)/He thermochronology precludes quantitative constraint on the temperature windows of cement precipitation and dissolution, relying instead on vitrinite reflectance (Ro) proxies that offer limited temporal resolution. (3) Numerical Modeling: Future work should integrate basin- and petroleum-system modeling to simulate the competing effects of mechanical compaction, quartz cementation kinetics, and feldspar dissolution rates under the path-dependent burial, quantifying the sensitivity of reservoir quality to variations in burial rate and geothermal gradient.

6. Conclusions

1. The Lower Cretaceous sandstones in the North Yellow Sea Basin evolved through a path-dependent diagenetic regime driven by polyphase Yanshanian–Himalayan burial. A prolonged erosional hiatus arrested early cementation, leaving the reservoir mechanically metastable. Subsequent rapid reburial triggered anomalous re-compaction, where mechanical processes dominated porosity loss (>80%), fundamentally decoupling reservoir quality from maximum burial depth.
2. Within this framework, reservoir heterogeneity is governed by facies-dependent susceptibility to re-compaction. Proximal matrix-supported gravels underwent pervasive pseudomatrix formation due to textural immaturity, rendering them non-reservoir. In contrast, channelized sandstones developed localized early calcite cement frameworks that buffered against mechanical compaction, preserving primary porosity that was later enhanced by feldspar dissolution to form exploration "sweet spots."
3. Effective reservoir prediction requires shifting from depth-porosity transforms to a diagenetic facies-based framework. This framework, validated by strong correlations between static well-log signatures and petrophysical properties, allows for precise targeting of favorable diagenetic facies (early-cemented, dissolution-enhanced channels) while avoiding compaction-dominated intervals. These insights provide a transferable model for evaluating porosity preservation in analogous polyphase-reactivated rift basins.

Author Contributions: X.Y.: Conceptualization, Methodology, Data Curation, Writing—Original Draft. J.L.: Conceptualization, Methodology, Writing—Review and Editing, Supervision. G.W.: Methodology, Visualization, Supervision. X.J.: Validation, Supervision. C.W.: Investigation and Supervision. H.W.: Resources. J.L. supervised the regional tectonic interpretation and conceptualized the re-compaction model; G.W. supervised the quantitative diagenetic assessment and reservoir quality prediction. Both authors contributed equally to the manuscript revision and act as co-corresponding authors. All authors have read and agreed to the published version of the manuscript.

Funding: This research was funded by National Natural Science Foundation of China Youth Fund (NO. 41302100), the project of China Geological Survey (No: DD20242406), Director's Foundation of GMGS (NO. 2024GMGS-QN-01) and the project of "Research on Petroleum Geological Conditions in Major Sedimentary Basins in southern SCS" (NO. 2024-NHYJ-037).

Data Availability Statement: The raw data are available on request from the author X.Y. (infiy@hotmail.com).

Acknowledgments: We are sincerely grateful to all colleagues who participated in sample collection and analytical testing, and we also extend our sincere thanks to the reviewers for their insightful comments and diligent work. This paper utilized Zhipu Qingyan (GLM-5.2) during the writing process for language polishing and grammatical proofreading. All research perspectives, experimental data, analytical results, and conclusions were independently completed by the author. The AI tool did not participate in research design, core argument construction, or the formulation of academic viewpoints. The author assumes full and independent academic responsibility for the entire content of this paper.

Conflicts of Interest: The authors declare no conflicts of interest.

References

1. Paxton, S.T.; Szabo, J.O.; Ajdukiewicz, J.M.; Klimentidis, R.E. Construction of an intergranular volume compaction curve for evaluating and predicting compaction and porosity loss in rigid-grain sandstone reservoirs. *AAPG (Am. Assoc. Pet. Geol.) Bull.* **2002**, *86*, 2047–2067. [CrossRef]
2. Allen, P.A.; Allen, J.R. *Basin Analysis: Principles and Application to Petroleum Play Assessment*, 3rd ed.; Wiley-Blackwell: Hoboken, NJ, USA, 2013; pp. 454–498.
3. Bloch, S.; Lander, R.H.; Bonnell, L. Anomalously high porosity and permeability in deeply buried sandstone reservoirs: Origin and predictability. *AAPG Bull.* **2002**, *86*, 301–328. [CrossRef]
4. Lundegard, P.D. Sandstone porosity loss; a "big picture" view of the importance of compaction. *J. Sediment. Res.* **1992**, *62*, 250–260. [CrossRef]
5. Wang, D.M.; Hu, J.M.; Zhang, Z.G. Kinematic history of the Tan-Lu fault zone constrained by the Late Mesozoic–Cenozoic tectono-sedimentary evolution of basins in the Luxi Block, eastern North China Craton. *J. Asian Earth Sci.* **2022**, *225*, 105041. [CrossRef]
6. Li, Z.Q.; Yang, B.; Han, Z.J. Tectonic-Thermal Evolution of Meso-Cenozoic Rift Basin in South Yellow Sea, Offshore Eastern China: Implications for Basin-Forming Mechanism and Thermal Evolution of Source Rocks. *Earth Sci.* **2022**, *47*, 1652–1668. [CrossRef]
7. Fu, S.; Yang, H.F.; Song, L.J. Tectono-sequence evolution of an extensional strike-slip composite basin, a case study of the Miaoxi'nan sub-sag in the eastern Bohai Bay Basin. *Mar. Pet. Geol.* **2025**, *171*, 107170. [CrossRef]
8. Morad, S.; Al-Ramadan, K.; Ketzer, J.M.; De Ros, L.F. The impact of diagenesis on the heterogeneity of sandstone reservoirs: A review of the role of depositional facies and sequence stratigraphy. *AAPG Bull.* **2010**, *94*, 1267–1309. [CrossRef]
9. Khalifa, M.A.; Morad, S. Impact of depositional facies on the distribution of diagenetic alterations in the Devonian shoreface sandstone reservoirs, Southern Ghadamis Basin, Libya. *Sediment. Geol.* **2015**, *329*, 62–80. [CrossRef]
10. Li, N.S. Tectonic evolution of three structural basins in the Yellow Sea. *Oceanol. Limnol. Sin.* **1995**, *26*, 354–362. (In Chinese)
11. Li, W.Y.; Li, D.X.; Wang, H.J. Research progress on structural geometry of the North Yellow Sea basin. *J. Geomech.* **2006**, *12*, 18–26. (In Chinese)
12. Li, W.Y.; Li, D.X.; Xia, B. Characteristics of Structural Evolution of the North Yellow Sea Basin. *Geosci. J. Grad. Sch. China Univ. Geosci.* **2006**, *20*, 268–276. (In Chinese)
13. Wang, G.Y.; Liu, J.P.; Jian, X.L. Proterozoic sedimentary sequences and zircon U-Pb dating in the East Sub-basin, North Yellow Sea. *J. Stratigr.* **2021**, *45*, 11–18. (In Chinese) [CrossRef]
14. Tian, Z.X.; Zhang, X.H.; Xue, R.J. Regional geologic features of the North Yellow Sea Basin. *Mar. Geol. Lett.* **2004**, *20*, 8–10. (In Chinese) [CrossRef]
15. Feng, Z.Q.; Yao, Y.J.; Zeng, X.H. New understanding of Mesozoic-Paleozoic tectonics and hydrocarbon potential in Yellow Sea. *China Offshore Oil Gas (Geol.)* **2002**, *16*, 367–373. (In Chinese)
16. Wang, G.Y.; Liu, J.P.; Jian, X.L.; Wang, H.J.; Du, M.; Wan, X.M. Characteristics and Genetic Mechanism of Tight Sandstone Reservoirs of Lower Cretaceous in North Yellow Sea Basin. *Earth Sci.* **2016**, *41*, 523–532. (In Chinese) [CrossRef]
17. Lin, C.S.; Zhang, Y.M.; Li, S.T.; Ren, J.Y.; Zhang, Y.Z. Episodic rifting dynamic process and quantitative model of Mesozoic Cenozoic faulted basins in eastern China. *Earth Sci.-J. China Univ. Geosci.* **2004**, *29*, 583–588. (In Chinese)

18. Liu, J.P.; Wang, G.Y.; Jian, X.L.; Zhu, C.Q.; Hu, X.Q.; Yuan, X.Q.; Wang, C. Tectono-thermal Mechanism and Hydrocarbon Generation Action in the North Yellow Sea Eastern Sub-basin. *Earth Sci. Front.* **2024**, *31*, 206–218. (In Chinese) [CrossRef]
19. Li, W.Y.; Zeng, X.H.; Huang, J.J. Meso-Cenozoic North Yellow Sea: Residual Basin or Superimposed Basin? *Acta Geol. Sin.* **2009**, *83*, 1269–1275. (In Chinese)
20. Dickinson, W.R. Interpreting Detrital Modes of Graywacke and Arkose. *J. Sediment. Petrol.* **1970**, *40*, 695–707. [CrossRef]
21. Atkins, J.E.; McBride, E.F. Porosity and packing of Holocene river, dune, and beach sands. *AAPG Bull.* **1992**, *76*, 339–355. [CrossRef]
22. Liu, J.P.; Wang, G.Y.; Wang, L.L.; Jian, X.L.; Du, M.; Wan, X.M. Main controlling, factors of hydrocarbon accumulation in the Eastern Sub-basin, North Yellow Sea. *Oil Gas. Geol.* **2015**, *36*, 888–896. [CrossRef]
23. Wang, R.F.; Chi, Y.G.; Zhang, L.; He, R.H.; Tang, Z.X.; Liu, Z. Comparative studies of microscopic pore throat characteristics of unconventional super-low permeability sandstone reservoirs: Examples of Chang 6 and Chang 8 reservoirs of Yanchang Formation in Ordos Basin, China. *J. Pet. Sci. Eng.* **2018**, *160*, 72–90. [CrossRef]
24. Yu, H.T.; Xu, Z.J.; Cheng, R.H.; Gao, D.; Zhang, Z. Response of Provenance Transition of Middle Jurassic–Early Cretaceous Sediments to Tectonic Domain Transformation in the North Yellow Sea Basin, Eastern North China Craton. *Geol. J.* **2022**, *57*, 1080–1109. [CrossRef]
25. Miall, A.D. *The Geology of Fluvial Deposits, Sedimentary Facies, Basin Analysis, and Petroleum Geology*; Springer: New York, NY, USA, 1996; pp. 75–190.
26. Blair, T.C.; McPherson, J.G. Alluvial fans and their natural distinction from rivers based on morphology, hydraulic processes, sedimentary processes, and facies assemblages. *J. Sediment. Res.* **1994**, *64*, 450–489. [CrossRef]
27. Miall, A.D. *Principles of Sedimentary Basin Analysis*, 3rd ed.; Springer: Berlin/Heidelberg, Germany, 2000; pp. 93–160.
28. Ramos, E.; Marzo, M.; de Gibert, J.M.; Tawengi, K.S.; Khoja, A.A.; Bolatti, N.D. Stratigraphy and sedimentology of the middle ordovician hawaz formation (Murzuq basin, Libya). *AAPG (Am. Assoc. Pet. Geol.) Bull.* **2006**, *90*, 1309–1336. [CrossRef]
29. Miall, A.D. A review of the braided-river depositional environment. *Earth Sci. Rev.* **1977**, *13*, 1–62. [CrossRef]
30. Miall, A.D. Lithofacies types and vertical profile models in braided river deposits: A summary. In *Fluvial Sedimentology*; Canadian Society of Petroleum Geologists: Calgary, AB, Canada, 1978; pp. 597–604.
31. Yu, H.T.; Xu, Z.J.; Cui, K.N.; Cheng, R.H.; Zhou, Y. Sedimentary Provenance Transition in the North Yellow Sea Basin During Tectonic Transition Period of the Eastern North China Craton in the Late Mesozoic and Its Tectonic Implications. *Geol. J.* **2025**, *60*, 2075–2094. [CrossRef]
32. Folk, R.L. *Petrology of Sedimentary Rocks*; Hemphill Publishing Company: Austin, TX, USA, 1980; pp. 25–178.
33. Hakimi, M.H.; Abdullah, W.H. Modelling petroleum generation of Late Cretaceous Dabut Formation in the Jiza-Qamar Basin, Eastern Yemen. *Mar. Pet. Geol.* **2015**, *61*, 1–13. [CrossRef]
34. Pittman, E.D.; Larese, R.E. Compaction of lithic sands: Experimental results and applications. *AAPG Bull.* **1991**, *75*, 1279–1299. [CrossRef]
35. Worden, R.H.; Morad, S. *Clay Minerals in Sandstones: Controls on Formation, Distribution and Evolution*; Wiley-Blackwell: Hoboken, NJ, USA, 2009.
36. Huang, D.; Yang, S.; Wu, Q.; Wu, Y.; Ma, S.; Zhang, Y. Diagenetic Characteristics and Evolution of Low-Permeability Clastic Reservoirs in the Mesozoic of the Tanhai Zone, Jiyang Depression. *Minerals* **2026**, *16*, 106. [CrossRef]
37. Bello, A.M.; Jones, S.J.; Gluyas, J.; Al-Ramadan, K. Impact of Grain-Coating Clays on Porosity Preservation in Paleocene Turbidite Channel Sandstones: Nelson Oil Field, UK Central North Sea. *Minerals* **2022**, *12*, 555. [CrossRef]
38. Gregg, J.M.; Howard, S.A.; Mazzullo, S.J. Early diagenetic recrystallization of Holocene. *Sedimentology* **1992**, *39*, 143–160. [CrossRef]
39. Ajdukiewicz, J.M.; Larese, R.E. How clay grain coats inhibit quartz cement and preserve porosity in deeply buried sandstones: Observations and experiments. *AAPG Bull.* **2012**, *96*, 2091–2119. [CrossRef]
40. Ehrenberg, S.N. Preservation of anomalously high porosity in deeply buried sandstones by grain-coating chlorite: Examples from the Norwegian. *Cont. Shelf* **1993**, *77*, 1260–1286. [CrossRef]
41. French, M.W.; Worden, R.H. Orientation of microcrystalline quartz in the Fontainebleau Formation, Paris Basin and why it preserves porosity. *Sediment. Geol.* **2013**, *284*, 149–158. [CrossRef]
42. Yuan, G.; Cao, Y.; Jia, Z. Selective dissolution of feldspars in the presence of carbonates: The way to generate secondary pores in buried sandstones by organic CO_2. *Mar. Pet. Geol.* **2015**, *60*, 105–119. [CrossRef]
43. Li, Y.; Xu, W.K.; Wu, P.; Meng, S.Z. Dissolution versus cementation and its role in determining tight sandstone quality: A case study from the Upper Paleozoic in northeastern Ordos Basin, China. *J. Nat. Gas. Sci. Eng.* **2020**, *78*, 103324. [CrossRef]
44. Dou, W.; Liu, L.; Wu, K.; Xu, Z.; Feng, X. Origin and significance of secondary porosity: A case study of Upper Triassic tight sandstones of Yanchang Formation in Ordos Basin, China. *J. Pet. Sci. Eng.* **2017**, *149*, 485–496. [CrossRef]
45. Li, W.H.; Hu, D.D.; Chang, Y.W.; Li, Y.N.; Guo, B.; Shi, Q.; Zhang, B. Diagenetic controls over reservoir quality of tight sandstone in the lower Jurassic reservoir in the Lenghu area, the north margin of Qaidam Basin. *Front. Earth Sci.* **2024**, *12*, 1298802. [CrossRef]

46. Wang, F.W.; Chen, D.X.; Wang, Q.C.; Shi, X.B.; Jiang, M.Y.; Du, W.L.; Li, S. Quantitative evaluation of sandstone carrier transport properties and their effects on hydrocarbon migration and accumulation: A case study of the Es_3^2 in the southern slope of Dongying Depression, Bohai Bay Basin. *Mar. Pet. Geol.* **2023**, *149*, 105978. [CrossRef]
47. Peltonen, C.; Marcussen, Ø.; Bjørlykke, K.; Jahren, J. Clay mineral diagenesis and quartz cementation in mudstones: The effects of smectite to illite reaction on rock properties. *Mar. Pet. Geol.* **2009**, *26*, 887–898. [CrossRef]
48. Zeng, H.L.; Hentz, T.F. High-Frequency Sequence Stratigraphy from Seismic Sedimentology: A Miocene Gulf Coast Example. *AAPG Bull.* **2004**, *88*, 153–174. [CrossRef]
49. Boulvais, P.; Vallet, J.M.; Estéoule-Choux, J. Origin of kaolinization in Brittany (NW France) with emphasis on deposits over granite: Stable isotopes (O, H) constraints. *Chem. Geol.* **2000**, *168*, 211–223. [CrossRef]

Disclaimer/Publisher's Note: The statements, opinions and data contained in all publications are solely those of the individual author(s) and contributor(s) and not of MDPI and/or the editor(s). MDPI and/or the editor(s) disclaim responsibility for any injury to people or property resulting from any ideas, methods, instructions or products referred to in the content.